



---

**Metal-ligand and Hydrogen Bonding in the Active Site of Fe(III)-, Mn(III)- and Co(III)-myoglobins**

Journal:	<i>Dalton Transactions</i>
Manuscript ID	DT-ART-11-2024-003246.R1
Article Type:	Paper
Date Submitted by the Author:	02-Jan-2025
Complete List of Authors:	Freindorf, Marek ; Southern Methodist University, Chemistry Kraka, Elfi; Southern Methodist University, Chemistry

**SCHOLARONE™**  
Manuscripts

# Journal Name

## ARTICLE TYPE

Cite this: DOI: 00.0000/xxxxxxxxxx

## Metal-ligand and Hydrogen Bonding in the Active Site of Fe(III)-, Mn(III)- and Co(III)-myoglobins<sup>†</sup>

Marek Freindorf,<sup>a</sup> and Elfi Kraka<sup>\*a</sup>

Received Date

Accepted Date

DOI: 00.0000/xxxxxxxxxx

We investigated in this work the strength of metal–ligand bonding in complexes formed between Fe(III)-, Mn(III)- and Co(III)-myoglobin and methanol, water, nitrite, and azide, serving as neutral and ionic prototype ligands, for the  $\varepsilon$  and  $\delta$  protonation forms of the myoglobin distal histidine. In total, 24 complexes and 12 associated gas phase models were investigated combining a QM/MM protocol with our local vibrational mode analysis at the PBE0/6-31g(d,p)/AMBER level of theory. According to our results, complexes with methanol and water ligands form weaker metal–ligand bonds than those with nitrite and azide ligands. Furthermore, the strength of the metal–ligand bonds depends on the protonation form of the distal histidine. Among the three metals investigated in this study, Fe, the metal found in native myoglobin, turned out to be the most versatile candidate, providing the broadest range of metal–ligand bond strengths. We also analyzed potential hydrogen bonds formed between the ligand and the distal histidine of the heme pocket. The  $\varepsilon$  tautomer of histidine forms weaker O···H type hydrogen bonds whereas the  $\delta$  tautomer forms stronger N···H type hydrogen bonds. Overall, our findings identify the strength of both metal–ligand and hydrogen bonds (fully captured by our local vibrational mode analysis) as a key parameter determining the catalytic activity and function of myoglobins. This is particularly relevant when considering neutral versus ionic ligands and other metals such as Mn or Co as alternatives to Fe. The insights gained through our investigation offer valuable guidance for strategically fine-tuning existing artificial myoglobins and designing new, versatile variants. We hope that our QM/MM - local mode analysis protocol will become a valuable addition to the research community's toolkit.

### 1 Introduction

Myoglobin (Mb) is a member of the hemoprotein superfamily, which is found in muscles of vertebrates and in almost all mammals. Mb is responsible for storage of oxygen in vertebrates and plays an important role in many physiological functions of the heart and skeletal muscles. It is also one of the most studied proteins disclosing interactions between the protein active site and the surrounding protein environment.<sup>1–4</sup> The active site of Mb includes a prosthetic heme group, which involves a protoporphyrin ring and a central Fe atom. The heme group is attached to the protein backbone by a covalent chemical bond with the proximal histidine, while the distal heme pocket can be occupied by small molecules such as O<sub>2</sub>, NO, H<sub>2</sub>S and CO, which are responsible for Mb's diverse biochemical activities.

Over the past decade a number of artificial Mb, i.e., functional-

ized, bioengineered, or synthetic Mb proteins have been reported being intended to adapt Mother Nature's unique design to the specific needs across chemistry and beyond with applications in catalysis potentially replacing less sustainable and environmental friendly industrial catalysts; such as in medicine helping maintain oxygen delivery in situations where blood transfusions are limited or unavailable,<sup>5</sup> or as biosensors detecting oxygen or other gases.<sup>6,7</sup> In addition, they are ideal research models in experiment and theory, providing a controlled model to study heme protein function, protein folding, and oxygen storage mechanisms.

There are a number of reports applying artificial Mbs to various challenging catalytic transformations, bridging the gap between the efficiency of enzymatic reactions and the versatility of transition metal catalysis. Iron porphycene complexes of Mb used for selective CH functionalization reactions offer innovative ways to form CC, CN and CO bonds, such as cyclopropanation, amination, and azide reduction.<sup>8–13</sup> The iron porphyrin cofactor makes heme proteins particularly well-suited as catalysts for nitrene transfer reactions, including the reduction of azides to amines.<sup>10</sup> An engineered Mb-based catalyst has shown to be capable of catalyzing the cyclopropanation of aryl-substituted olefins with cat-

<sup>a</sup> Chemistry Department, Southern Methodist University, 3215 Daniel Avenue, Dallas, TX 75275, USA; E-mail: ekraka@smu.edu

<sup>†</sup> Supplementary Information available: plots of additional properties of HBs in the investigated protein systems, pictures of active sites in the proteins and the gas phase, and optimized coordinates of the active sites. See DOI: 00.0000/00000000.

alytic proficiency and excellent diastereo- and enantioselectivity via transmetalation.<sup>14</sup>

Replacement of Fe in hemoproteins by different transition metals has been utilized to investigate the role of heme in determining the protein properties for many years,<sup>15–17</sup> and the most popular metals used in the modified hemoproteins are Mn and Co.<sup>18,19</sup> Some recent examples of the Mn–substituted Mb (MnMb) include the discovery of two redox pathways in MnMb,<sup>20</sup> CH bond hydroxylation catalyzed in MnMb,<sup>21,22</sup> and oxidation properties of MnMb towards weak CH bonds.<sup>23</sup> Similarly, examples of Mn–substituted cytochromes P450 include structural properties of Mn–substituted P450(CYP101),<sup>24</sup> theoretical study of the pentacoordinate Mn in cytochrome P450<sub>cam</sub>,<sup>25</sup> catalytic activity of Mn–substituted cytochrome P450(BSB),<sup>26</sup> reconstruction of Mn–substituted cytochrome P450(BM3).<sup>27–29</sup> The Mn metal was also used in Mn–substitution of an biological protein in a study of a porphyrin-binding protein with high–valent Mn oxidation states.<sup>30</sup>

Similarly, recent examples of Co–substituted Mb (CoMb) involve theoretical study of dioxygen bound to CoMb,<sup>31</sup> relaxation of ligand binding in CoMb,<sup>32</sup> nitrogen generation in CoMb,<sup>33</sup> and reconstruction of aqua– and cyano–CoMb.<sup>34</sup> Cobalt was also used in metal–substituted cystathionine  $\beta$ –synthase,<sup>35</sup> hydrogen generation from Co–substituted microperoxidase–11<sup>36</sup> and cytochrome b<sub>562</sub>,<sup>37</sup> reconstruction of CoMb–coupled histidine kinase<sup>38</sup>, and Co–substitution in a series of hemoproteins in living cells of *E. coli*.<sup>39</sup> CoMb complexes were used to catalyze electro–catalytic H<sub>2</sub> evaluation.<sup>40,41</sup> Heme oxygenase cobalt–protoporphyrin complexes were used for CO<sub>2</sub> photoreduction.<sup>42</sup> The Figg group has also introduced zinc–Mbs as catalyst for photo–induced electron/energy transfer (PET)–reversible addition–fragmentation chain transfer (RAFT) polymerizations.<sup>43</sup>

In order to systematically explore the large potential of these Fe, Co, Mn–Mbs, fine–tuning them for a specific purpose and/or the development of new design routes for artificial Mbs, the understanding of metal–ligand (ML) and potential ligand–hydrogen bonding (HB) in the active Mb pocket at the molecular level is an important prerequisite, which to our best knowledge has been missing so far.

Therefore, inspired by the structural study of Mn– and Co–substituted Mb,<sup>18</sup> we explored in this study similarities or differences between native Fe(III)Mb, and the engineered Mn(III)Mb and Co(III)Mb systems with methanol (CH<sub>3</sub>OH, MET), water (H<sub>2</sub>O, H<sub>2</sub>O), nitrite (NO<sub>2</sub><sup>–</sup>, ONO), and azide (N<sub>3</sub><sup>–</sup>, NNN) model ligands in the distal heme pocket, with a focus on assessing and comparing the strength of the ML bonds and the strength of potential HB interactions, formed between the distal histidine and the ligands. In order to account for the influence of the protein environment, we compared the ML bond strengths in the proteins with those of corresponding gas phase models. Sketches of the active sites of Fe(III)Mb, Mn(III)Mb and (Co(III)Mb with the four ligands as well the corresponding active site gas phase models, investigated in this work, are presented in Figure 1. As revealed in Figure 1, in the six of the investigated protein systems the ligand forms either an O···H or an N···H HB with the distal histidine, which we com-

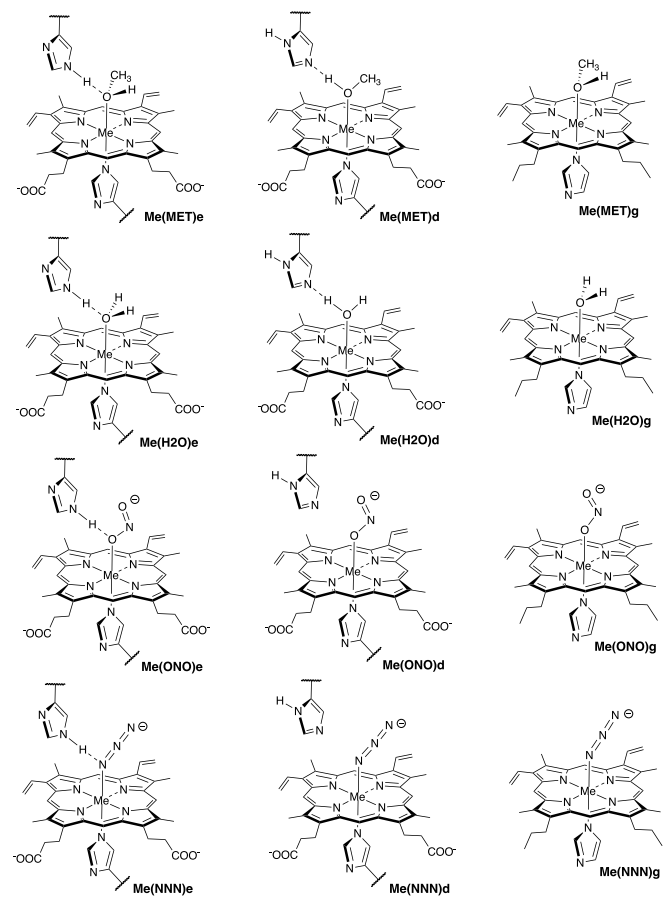


Fig. 1 Sketches of active sites in MB and gas phase models with ligands investigated in this study (Me = Fe, Mn, and Co). Symbols "e" and "d" indicate distal histidine in  $\varepsilon$  and  $\delta$  protonation forms, respectively, while symbol "g" indicates gas phase models. For molecular labels, see text.

pared with the corresponding HB strengths in the water dimer (H<sub>2</sub>OHOH) and the water–ammonia pair (HOHNH<sub>3</sub>). Two tautomeric forms of distal histidine were considered, namely His64 $\varepsilon$  and His64 $\delta$  (labeled in the following as "e" and "d"), which led to 24 protein complexes and 12 gas phase models. A special focus of this work was on exploring the relevance of the strength of these ML/HB interactions regarding catalytic activity or function of these Mbs for neutral versus ionic ligands as well as for Co and Mn substituted Fe-heme co-factors.

The following complex notation is used throughout the manuscript (see also Figure 1): (i) iron complexes: Fe(MET)e, Fe(MET)d, Fe(H<sub>2</sub>O)e, Fe(H<sub>2</sub>O)d, Fe(ONO)e, Fe(ONO)d, Fe(NNN)e, and Fe(NNN)d; (ii) manganese complexes: Mn(MET)e, Mn(MET)d, Mn(H<sub>2</sub>O)e, Mn(H<sub>2</sub>O)d, Mn(ONO)e, Mn(ONO)d, Mn(NNN)e, and Mn(NNN)d; (iii) cobalt complexes: Co(MET)e, CoMb(MET)d, Co(H<sub>2</sub>O)e, Co(H<sub>2</sub>O)d, Co(ONO)e, Co(ONO)d, Co(NNN)e, and Co(NNN)d; (iv) corresponding heme co-factor ligand gas phase models: Fe(MET)g, Fe(H<sub>2</sub>O)g, Fe(ONO)g, and Fe(NNN)g; Mn(MET)g, MnMb(H<sub>2</sub>O)g, Mn(ONO)g, and Mn(NNN)g; and Co(MET)g, Co(H<sub>2</sub>O)g, Co(ONO)g, and Co(NNN)g. We utilized for the protein calculations a hybrid QM/MM (quantum mechanics –

molecular mechanics) ansatz,<sup>44–48</sup> and for the bond strength assessment we used the local vibrational mode theory (LMA) developed in our group,<sup>49,50</sup> complemented with Bader's quantum theory of atoms in molecules (QTAIM) analysis<sup>51–53</sup> and natural bond orbital (NBO) analysis.<sup>54,55</sup>

## 2 Materials and Methods

### 2.1 Local vibrational mode analysis

In order to assess and compare ML and HB in the Mb complexes investigated in this work a qualified bond strength descriptor is needed. One popular measure to assess bond strength is to use normal mode stretching force constants derived from a normal mode analysis.<sup>56</sup> However, as pointed out by Wilson in his pioneering 1941 publication<sup>57</sup> normal vibrational modes of polyatomic molecules are generally delocalized, limiting this approach. LMA<sup>49,50</sup> originally developed by Konkoli and Cremer<sup>58,59</sup> has solved this problem via extracting local vibrational modes and corresponding local mode force constant from the normal vibrational modes.

A local vibrational mode  $\mathbf{a}_n$  is defined as

$$\mathbf{a}_n = \frac{\mathbf{K}^{-1} \mathbf{d}_n^\dagger}{\mathbf{d}_n \mathbf{K}^{-1} \mathbf{d}_n^\dagger} \quad (1)$$

The two ingredients needed for LMA, the diagonal normal mode force constant matrix  $\mathbf{K}$  in normal mode coordinates  $\mathbf{Q}$  and the normal mode vectors  $\mathbf{d}_n$  in internal coordinates, can be obtained from a vibrational frequency calculation via the Wilson GF formalism,<sup>60,61</sup> which is a routine part of most modern quantum chemistry packages.<sup>62</sup> As a consequence, LMA can be applied with minimal computational costs after a routine quantum-chemical calculation of vibrational frequencies, optionally adding measured frequencies as input (a feature opening LMA to the experimental vibrational spectroscopists) to both single molecules in gas phase, solution, or in a protein, but also to periodic systems and crystals.<sup>49,50</sup>

For each local mode  $\mathbf{a}_n$ , one can derive associated local force constants  $k_n^a$  describing the local vibration of the atomic fragment under consideration,

$$k_n^a = \mathbf{a}_n^\dagger \mathbf{K} \mathbf{a}_n = \frac{1}{\mathbf{d}_n \mathbf{K}^{-1} \mathbf{d}_n^\dagger} \quad (2)$$

local mode frequencies, local mode infrared intensities and other local properties can be determined.<sup>50,63</sup>

Over the past two decades, we have successfully applied local mode force constants to characterize the strength of covalent bonds and non-covalent interactions across the periodic table as documented in two recent review articles,<sup>49,50</sup> including bonding inside the active sites of hemoproteins.<sup>64–71</sup> Another important feature of LMA is the characterization of normal mode (CNM) procedure, which decomposes each normal vibrational mode into local mode contributions.<sup>49,50,72,73</sup> CNM has advanced the interpretation of vibrational spectra to the next level e.g., identifying which molecular fragments couple in DNA–base pairs or assessing the quality of Stark effect probes with a local probe bond, just to name two examples.<sup>67,74–76</sup> A detailed description of the un-

derlying local vibrational mode theory can also be found in the two review articles.<sup>49,50</sup>

In this work we predominantly focused on local mode stretching force constants  $k^a(AB)$  reflecting the intrinsic strength the bond/weak interaction between two atoms A and B,<sup>77</sup> applied to ML and ligand–histidine HB. For easier comparison we transformed the local mode force constants  $k^a(AB)$  into relative bond strength orders (BSO) according to the generalized Badger rule derived by Cremer, Kraka, and coworkers<sup>78,79</sup> via a power relationship in the form of  $BSO = x(k^a)^y$ . Two reference molecules with known BSO and force constants are utilized to obtain the parameters for  $x$  and  $y$ , with the constraint that a zero value for the force constant  $k^a(AB)$  equals a zero BSO value. The reference molecules utilized in our study are presented in Table 1. For the Me–ligand bonds we referred to Mayer's bond orders<sup>80–82</sup> instead of using BSO=1 for single and BSO=2 for double bonds, which in past studies involving transition metal bonding have turned out to be a better choice.<sup>49,50,64,68,83</sup>

Table 1 Bond length R, local mode force constant  $k^a$ , and bond strength order BSO of selected bonds in reference molecules used in our study

Bond	R(Å)	$k^a$ (mDyn/Å)	BSO <sup>1</sup>	Molecule
M–C	1.792	3.243	1.005	CuCH <sub>3</sub>
M=C	1.641	5.568	1.894	NiCH <sub>2</sub>
N–H, O–H	1.142 0.920	1.340 9.804	0.500 1.000	F <sub>2</sub> H <sup>–</sup> FH

<sup>1</sup> BSO values of bonds involving metal atoms are based on Mayer's bond orders<sup>80–82</sup>

We complemented LMA with features of the analysis of the electron density  $\rho(\mathbf{r})$  via Bader's QTAIM theory.<sup>51–53</sup> In particular the covalent character of the ML and HBs were determined via the Cremer–Kraka criterion<sup>84,85</sup>, which is based on the local electron density  $H(\mathbf{r}) = G(\mathbf{r}) + V(\mathbf{r})$ , where the kinetic energy density is  $G(\mathbf{r})$  (positive, destabilizing) and the potential energy density is  $V(\mathbf{r})$  (negative, stabilizing). If at the bond critical point  $\mathbf{r}_b$  of  $\rho(\mathbf{r})$  between two bonded atoms AB  $H(\mathbf{r}_b)$  is negative, the character of AB bond is predominantly covalent, whereas a positive  $H(\mathbf{r}_b)$  value indicates a predominantly electrostatic character. In addition we analyzed the atomic NBO charges in ML and HB.<sup>54,86</sup>

### 2.2 Calculational details

The starting geometries for the Mn(III)Mb protein systems with methanol (CH<sub>3</sub>OH), water (H<sub>2</sub>O), nitrite (NO<sub>2</sub><sup>–</sup>), and azide (N<sub>3</sub><sup>–</sup>) ligands placed in the distal heme pocket (see Figure 1) were taken from the horse heart X-ray structures of oxidized manganese substituted myoglobin with methanol (PDB entry: 2O5L), water (PDB entry: 2O58), nitrite (PDB entry: 2O5O), and azide (PDB entry: 2O5M) ligands in the distal heme pocket.<sup>18</sup> The starting geometries for the Fe(III)Mb and Co(III)Mb protein systems were obtained from the corresponding Mn(III)Mb complexes by manually substituting the Mn metal center with Fe and Co, respectively. For all eight complexes hydrogen atoms were added to the experimental protein structures and the proteins were neutralized by counter-ions using AMBER.<sup>87</sup> In order to simulate a water environment, the active sites of the proteins were surrounded by a sphere of TIP3P water molecules,<sup>88</sup> with a radius of 16 Å. Af-

ter initial minimization with AMBER, the protein systems were divided into a QM part including the heme co-factor, distal and proximal histidine side chains of Mb, and the ligand (ca. 110 atoms), while the MM part included remaining protein atoms (ca. 3000 atoms) as well as water molecules. Based on previous work on Mb<sup>64,68</sup> and supported by the finding of others reporting that the PBE0 functional<sup>89,90</sup> DFT shows good performance for the calculation of transition metals complexes,<sup>91-94</sup> we used for the QM/MM calculations PBE0 in combination with Pople's 6-31G(d,p) basis set.<sup>95</sup> For the MM part we applied the AMBER force field.<sup>87</sup> The QM/MM geometry optimization and frequency calculations were performed with scaled electronic embedding using the ONIOM method.<sup>96</sup> All QM/MM geometry optimizations finished as local minima on the potential energy surface, i.e., no imaginary normal mode frequencies were found. The calculations in the gas phase were done in this study using the PBE0/6-31G(d,p) level of theory. Using this model chemistry, the calculated FeN bond length of 1.965 Å in the ferric state turned out to be close to the X-ray bond length in bis(1-methylimidazole) (meso-tetramesitylporphinato) Fe(III) (1.970 Å).<sup>97</sup>

Our previous calculations on Fe(III)Mb systems<sup>68</sup> in line with experimental data on an Fe(III)Mb–water ligand complex<sup>98,99</sup> suggest that the heme co-factor is a high-spin species. Therefore, we calculated Fe(III)Mb complexes with the neutral ligands (i.e., water and methanol) in their quartet electronic state ( $S = 3/2$ ). In contrast, experimental data on Fe(III)Mb complexes with ionic ligands (i.e., nitrite and azide) suggest a low-spin heme co-factor.<sup>100-102</sup> Following this suggestion, we calculated Fe(III)Mb complexes with the nitrite and azide ligands in their doublet electronic state ( $S = 1/2$ ). Similarly, following suggestions based on experimental data, the Mn(III)Mb protein systems were calculated in this study as high-spin species ( $S = 2$ ),<sup>23,103</sup> and Co(III)Mb protein systems as low-spin species ( $S = 0$ ).<sup>32</sup> Geometry optimizations and vibrational frequency calculations were performed with Gaussian16,<sup>104</sup> the LMA analysis was performed using our LModeA program,<sup>105</sup> The QTAIM analysis was performed with the AIMALL program<sup>106</sup> and NBO charges were calculated utilizing the NBO analysis implemented in Gaussian16. In the following, we present the results of our calculations to three decimal places for most bond properties investigated in this study. To justify this level of accuracy, we performed calculations for **Fe(MET)e** and **Fe(MET)d** using the B3LYP/6-311G(d,p)/AMBER level of theory, and a comparison with the PBE0/6-31G(d,p)/AMBER method is provided in Table S1 on page S4 of the Supporting Information. Additionally, we compared the PBE0/6-31G(d,p)/AMBER level of theory with PBE0/def2-TZVP/SDD(Fe)/AMBER, and the results are presented in Table S7 on page S5 of the Supporting Information. Table S2 on page S4 of the Supporting Information shows a comparison of theoretical bond lengths for the heme group in **Mn(MET)e** and **Mn(MET)d** with experimental data (PDB entry: 2O5L). Moreover, Tables S3 and S4 on page S5 of the Supporting Information show the results of calculations for **Fe(MET)e** and **Fe(MET)d** using the PBE0/6-31G(d,p)/AMBER level of theory in the doublet, quartet, and sextet electronic states.

### 3 Results and discussion

In the following ML bonding is discussed for the Fe(III)Mb–ligand complexes and their gas phase analogues, followed by Mn(III)Mb–ligand bonding and Co(III)Mb–ligand bonding. In addition to forming chemical bonds with the metal of the heme co-factor, there is also the opportunity for HB formation with the distal histidine for six protein ligand complexes, as shown in Figure 1. This will be elucidated in the following sections for the Fe, Co, and Mn protein complexes.

Table 2 Bond length R, local mode force constant  $k^a$ , energy density at bond critical point  $H_p$ , charge difference  $\Delta q$ , and bond strength order BSO of ML bonds in Fe(III)Mb proteins along with gas phase models investigated in our study; for molecular labels, see text.

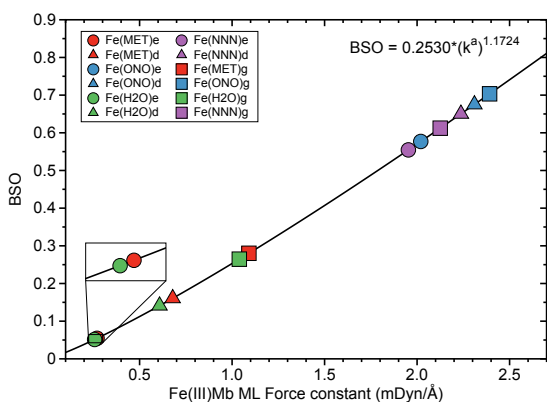
Molecule	Bond	R Å	$k^a$ mDyn/Å	$H_p$ Hr/Bohr <sup>3</sup>	$\Delta q$ e	BSO
<b>Fe(MET)e</b>	FeO	2.398	0.270	-0.0059	2.194	0.055
<b>Fe(MET)d</b>	FeO	2.140	0.679	-0.0062	2.257	0.161
<b>Fe(ONO)e</b>	FeO	1.881	2.020	-0.0082	1.691	0.577
<b>Fe(ONO)d</b>	FeO	1.852	2.310	-0.0141	1.627	0.675
<b>Fe(H2O)e</b>	FeO	2.409	0.257	-0.0054	2.218	0.051
<b>Fe(H2O)d</b>	FeO	2.184	0.608	-0.0068	2.400	0.141
<b>Fe(NNN)e</b>	FeN	1.911	1.953	-0.0232	1.671	0.555
<b>Fe(NNN)d</b>	FeN	1.875	2.237	-0.0322	1.557	0.650
<b>Fe(MET)g</b>	FeO	1.992	1.091	0.0023	1.942	0.280
<b>Fe(ONO)g</b>	FeO	1.846	2.392	-0.0146	1.629	0.703
<b>Fe(H2O)g</b>	FeO	2.010	1.039	0.0030	2.084	0.265
<b>Fe(NNN)g</b>	FeN	1.884	2.125	-0.0277	1.546	0.612

#### 3.1 ML bonds in Fe(III)Mb

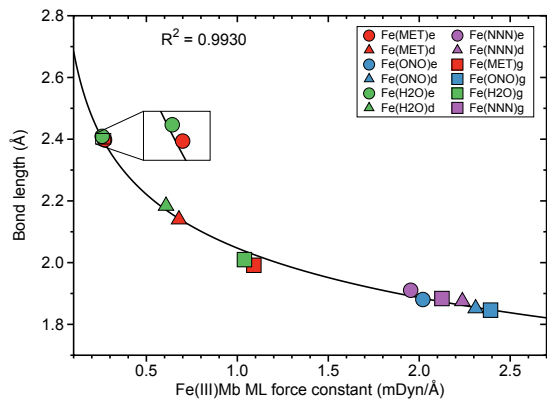
Fe–ligand bond properties of the investigated Fe(III)Mb–ligand complexes and the corresponding gas phase models are presented in Table 2. Relationships between these properties are shown in Figures 2 and 3.

According to Figure 2a, the Fe–ligand bond strengths clusters into two groups; one group for systems with the two neutral ligands, methanol (**Fe(MET)e**, **Fe(MET)d**, and **Fe(MET)g**, with an average  $k^a$  value of 0.680 mDyn/Å) and water (**Fe(H2O)e**, **Fe(H2O)d**, and **Fe(H2O)g**, with an average  $k^a$  value of 0.635 mDyn/Å). The other group involving the two ionic ligands, nitrite (**Fe(ONO)e**, **Fe(ONO)d**, and **Fe(ONO)g**, with an average  $k^a$  value of 2.241 mDyn/Å) and azide (**Fe(NNN)e**, **Fe(NNN)d**, and **Fe(NNN)g**, with an average  $k^a$  value of 2.105 mDyn/Å). Overall, ionic ligands are characterized by considerably stronger Fe–ligand bonding with BSO values between 0.6 and 0.7, whereas as neutral ligands lead to weak Fe–ligand bonds with BSO values in the range of 0.05 – 0.25. Interesting to note is that for ionic ligands BSO values for proteins and gas phase reference Fe–ligand bonds are comparable whereas for neutral ligands gas phase values are at the stronger end. Moreover, the strength of the Fe–ligand bond in the proteins for the  $\epsilon$  protonation form is smaller than for the  $\delta$  protonation form.

Figure 2b shows the relationship between the local mode force constant  $k^a$  and the bond length R for the molecular systems involving the Fe–ligand chemical bond. According to this Figure the stronger bond generally correlates well ( $R^2 = 0.9930$ ) with the smaller bond length, which is consistent with the Badger



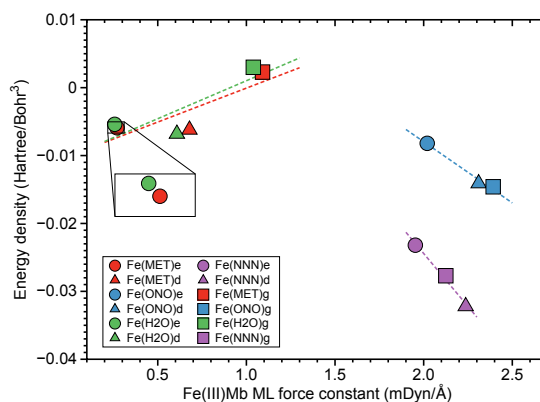
(a)



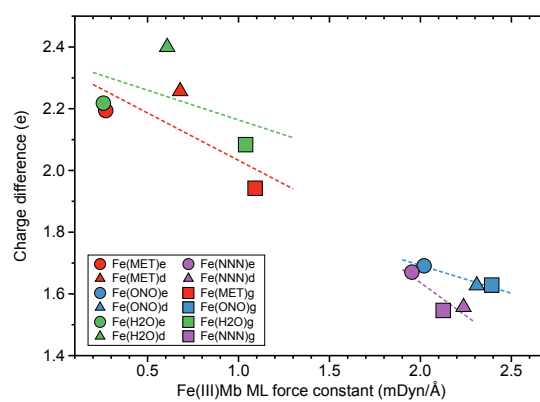
(b)

Fig. 2 Properties of ML bonds in Fe(III)Mb complexes and corresponding gas phase models. a) Bond strength order BSO calculated from local mode force constants  $k^a$  via the generalized Badger rule. b) Relation between local mode force constant  $k^a$  and bond length R. For molecular labels, see text.

rule.<sup>79,107</sup> The covalent character of this bond is expressed in our study by the energy density at the bond critical point  $H_p$ , where the more negative value of the energy density indicates on a more covalent bond character. The relation between those two quantities is presented in Figure 3a. We find three clusters formed by the individual ligands investigated in this study. The average energy density for the molecular systems with methanol has an  $H_p$  value of -0.0032 Hartree/Bohr<sup>3</sup>, which indicates on a small covalent character of this bond, similarly as for the molecular systems with water where the average energy density has an  $H_p$  value of -0.0031 Hartree/Bohr<sup>3</sup>. The Fe-ligand chemical bond has more pronounced covalent character for the molecular systems with the ionic ligands. The average energy density for the molecular systems with nitrite has an  $H_p$  value of -0.0123 Hartree/Bohr<sup>3</sup>, while for the systems with azide it has an  $H_p$  value of -0.0277 Hartree/Bohr<sup>3</sup>. Figure 3c shows the relation between the local mode force constant  $k^a$  and the charge difference  $\Delta q$  between the Fe atomic charge and the O or N atomic charge of the ligand. Similar as in Figure 3a, we find three clusters in Figure 3b formed by the individual ligands. Larger charge differences are observed for molecular systems with water (an average  $\Delta q$  value of 2.234 e), and with methanol (an average  $\Delta q$  value of 2.131 e), and smaller



(a)



(b)

Fig. 3 Properties of ML bonds in Fe(III)Mb complexes and corresponding gas phase models. a) Relation between local mode force constant  $k^a$  and energy density  $H_p$ . b) Relation between local mode force constant  $k^a$  and atomic charge difference. For molecular labels, see text.

for systems with nitrite (an average  $\Delta q$  value of 1.649 e) and azide (an average  $\Delta q$  value of 1.591 e).

### 3.2 ML bonds in Mn(III)Mb

ML bond properties of the Mn(III)Mb-ligand complexes and the corresponding gas phase models are presented in Table 3. Relationships between these properties are shown in Figures 4 and 5.

According to Figure 4a, the Mn-ligand bonds cluster into two groups, one with neutral ligands and one with ionic ligands. The molecular systems with the water ligand have an average force constant  $k^a$  of 0.354 mDyn/Å. Similarly as for systems with Fe-ligand bonds, the strength of the Mn-ligand bond in the protein is smaller for the  $\epsilon$  protonation form of distal histidine than in the  $\delta$  form. The strength of the Mn-ligand bond in the systems with methanol is widely distributed keeping a small value for the gas phase model ( $k^a$  of a value of 0.365 mDyn/Å), through a medium value for the  $\epsilon$  protein system ( $k^a$  of a value of 0.949 mDyn/Å), to a relatively big value for the  $\delta$  protein system ( $k^a$  of a value of 1.612 mDyn/Å). Both molecular systems with the ionic ligands have a medium strength, with the average value of the force constant  $k^a$  of a value of 1.062 mDyn/Å for the system with nitrite, and a value of 1.138 mDyn/Å for the system with azide. How-

Table 3 Bond length R, local mode force constant  $k^a$ , energy density at bond critical bond  $H_p$ , charge difference  $\Delta q$ , and bond strength order BSO of ML bonds in Mn(III)Mb proteins along with gas phase models investigated in our study; for molecular labels, see text

Molecule	Bond	R	$k^a$	$H_p$	$\Delta q$	BSO
		Å	mDyn/Å	Hr/Bohr <sup>3</sup>	e	
Mn(MET)e	MnO	2.070	0.949	-0.0029	2.272	0.238
Mn(MET)d	MnO	1.961	1.612	0.0010	2.322	0.443
Mn(ONO)e	MnO	2.128	0.887	-0.0042	2.131	0.220
Mn(ONO)d	MnO	2.048	1.036	-0.0032	2.084	0.264
Mn(H2O)e	MnO	2.492	0.224	-0.0047	2.492	0.044
Mn(H2O)d	MnO	2.268	0.485	-0.0046	2.532	0.108
Mn(NNN)e	MnN	2.141	0.898	-0.0100	2.144	0.223
Mn(NNN)d	MnN	2.011	1.392	-0.0103	2.014	0.373
Mn(MET)g	MnO	2.352	0.365	-0.0051	2.317	0.078
Mn(ONO)g	MnO	2.038	1.263	-0.0047	2.099	0.333
Mn(H2O)g	MnO	2.362	0.353	-0.0049	2.485	0.075
Mn(NNN)g	MnN	2.054	1.124	-0.0122	2.046	0.290

ever, the average strength of the Mn-ligand bonds ( $k^a$  of a value of 0.882 mDyn/Å), is smaller than the average strength of the Fe-ligand bonds ( $k^a$  of a value of 1.415 mDyn/Å). For the neutral ligands forming the bond with Mn, the BSO values range between 0.05 and 0.1, and the BSO values for the ionic ligands are in the range of 0.2 – 0.45, i.e., they show a larger spread than their Fe-ligand counterpart. According to Figure 4b, the local mode force constant  $k^a$  of the Mn-ligand bond relatively good correlates ( $R^2 = 0.9897$ ) with the bond length R, and according to Figure 5a, the Mn-ligand bonds in all systems have a covalent character, confirmed by negative values of the energy density (an average  $H_p$  value of -0.0047, -0.0040, and -0.0108 Hartree/Bohr<sup>3</sup>, for the systems with water, nitrite, and azide, respectively), with one exception. The Mn-ligand bond shows electrostatic character for the  $\delta$  protein system with methanol ( $H_p$  of a value of 0.0010 Hartree/Bohr<sup>3</sup>), which is also the strongest Mn-ligand bond ( $k^a$  of a value of 1.612 mDyn/Å). According to Figure 5b, the largest atomic charge difference of the Mn-ligand bond is observed in our calculations for molecular systems with water (an average  $\Delta q$  value of 2.503 e), and the smallest values are observed for both systems with the ionic ligands (the average  $\Delta q$  value of 2.105 and 2.068 e, for the system with nitrite and azide, respectively). The charge difference for the system with methanol has a medium value (an average  $\Delta q$  value of 2.304 e).

### 3.3 ML bonds in Co(III)Mb

Co-ligand bond properties of the Co(III)Mb-ligand complexes and the corresponding gas phase models are presented in Table 4. Relationships between these properties are shown in Figures 6 and 7. According to Figure 6a, the Co-ligand bond strengths can be grouped into two clusters, one representing the weaker neutral Co-ligand bonds and one with the stronger Co-ligand ionic bonds, i.e., we find the same trends as for the Fe and Mn systems. The Co-ligand bond strength for the systems with the neutral ligands is substantially smaller (average  $k^a$  value of 1.262 and 1.273 mDyn/Å, for water and methanol, respectively) than for the systems with the ionic ligands (average  $k^a$  value of 2.298 and 2.063 mDyn/Å, for nitrite and azide, respectively). However, in contrast to the Fe-ligand bonds, we find a larger spread for the neutral

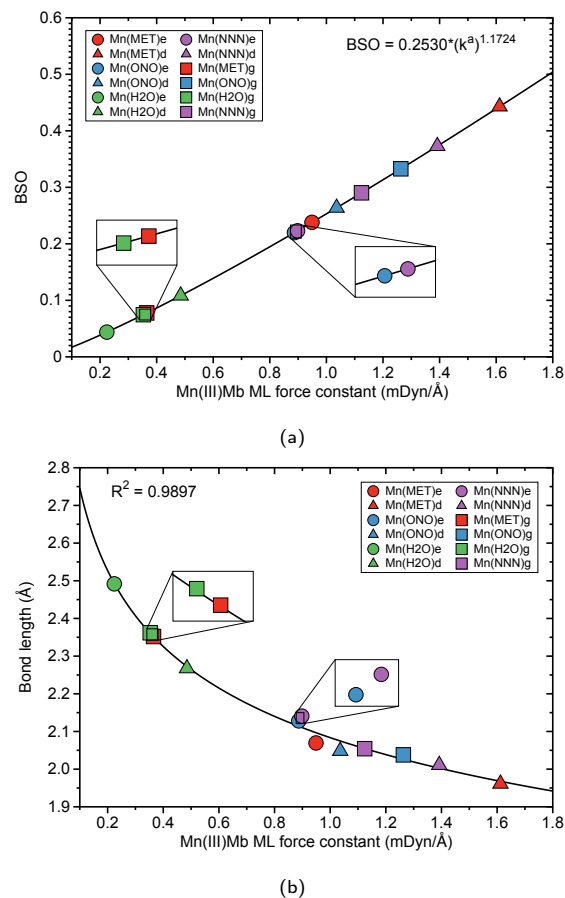
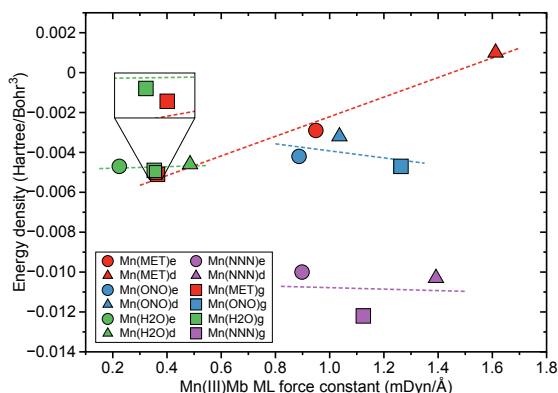


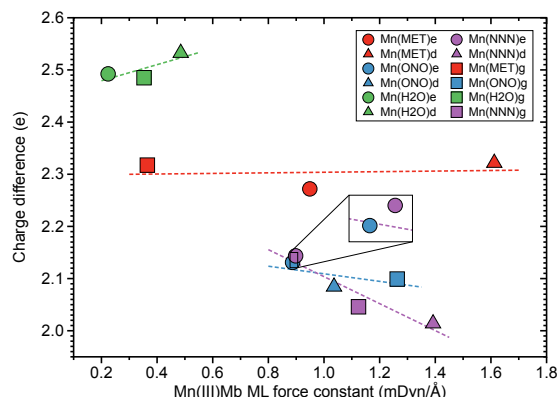
Fig. 4 Properties of ML bonds in Mn(III)Mb-ligand complexes and corresponding gas phase models. a) Bond strength order BSO calculated from local mode force constants  $k^a$  via the generalized Badger rule b) Relation between local mode force constant  $k^a$  and bond length R. For molecular labels, see text.

system with the BSO range between 0.2 – 0.45 for the neutral ligands, and 0.5 – 0.7 for the ionic ligands, respectively. Similarly as in the Fe-ligand bonds, the strength of the Co-ligand bond in the  $\epsilon$  protein conformer is smaller than that in the  $\delta$  conformer. Overall, the average strength of the Co-ligand bonds (average  $k^a$  of a value of 1.724 mDyn/Å) is larger than the average strength of the Fe-ligand bonds (average  $k^a$  of a value of 1.415 mDyn/Å) and that of the Mn-ligand bonds (average  $k^a$  of a value of 0.882 mDyn/Å).

According to Figure 6b, Co-ligand local mode force constants  $k^a$  correlate well with the Co-ligand bond lengths R ( $R^2 = 0.9710$ ). Figure 7a reveals that, similarly as found for the Fe systems, the neutral Co-ligand bonds have an energy density  $H_p$  which is close to zero (an average  $H_p$  value of 0.0002 and -0.0006 Hartree/Bohr<sup>3</sup>, for water and methanol, respectively), indicating on a predominant electrostatic character of this bond. However, the systems with the ionic Co-ligand bonds display a covalent character (average  $H_p$  value of -0.0131 and -0.0289 Hartree/Bohr<sup>3</sup>, for nitrite and azide, respectively). As shown in Figure 7b, we find a similar relationship between the atomic charge difference  $\Delta q$  and the local mode force constant  $k^a$  for the Co-ligand bonds as for the systems involving the Fe-ligand bonds.



(a)



(b)

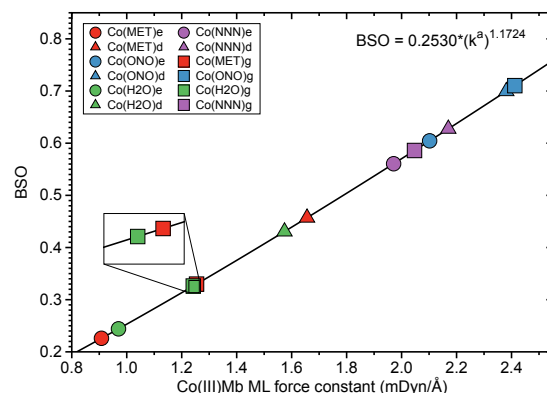
Fig. 5 Properties of ML bond in Mn(III)Mb–ligand complexes and corresponding gas phase models. a) Relation between local mode force constant  $k^a$  and energy density  $H_p$ . b) Relation between local mode force constant  $k^a$  and atomic charge difference. For molecular labels, see text.

The charge difference between the Co and ligand atoms for the neutral ligands is relatively big (average  $\Delta q$  value of 1.912 and 1.787 e, for water and methanol, respectively), when compared to the charge differences for the systems involving the ionic ligands (average  $\Delta q$  value of 1.465 and 1.409 e, for nitrite and azide, respectively).

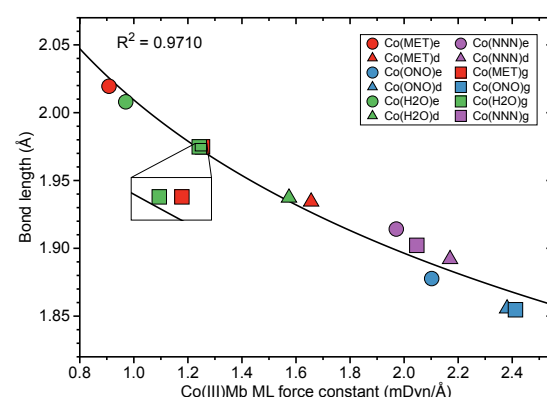
### 3.4 Protein–ligand hydrogen bonding

As depicted in Figure 1, in six of the investigated Mb–ligand complexes, the ligand can form a HB with the distal histidine, namely in **Me(MET)e**, **Me(MET)d**, **Me(H2O)e**, **Me(H2O)d**, **Me(ONO)e**, and **Me(NNN)e**. The  $\epsilon$  form of the distal histidine serves as HB donor leading to O···H type HBs with the ligand for **Me(MET)e**, **Me(H2O)e**, and **Me(ONO)e**, and for **Me(NNN)e** to an N···H type HB. The  $\delta$  form of the distal histidine serves as HB acceptor leading to N···H type HBs with the ligand for **Me(MET)d** and **Me(H2O)d**.

Table 5 shows HB properties for the MeMb–ligand complexes ( $\text{Me} = \text{Fe, Mn, Co}$ ) along with HB properties of the water dimer ( $\text{H}_2\text{OHOH}$ ) and the water–ammonia pair ( $\text{HOHNH}_3$ , where water is a hydrogen atom donor) for comparison. Figures 8, 9, and



(a)



(b)

Fig. 6 Properties of ML bonds in Co(III)Mb–ligand complexes and corresponding gas phase models. a) Bond strength order BSO calculated from local mode force constants  $k^a$  via the generalized Badger rule. b) Relation between local mode force constant  $k^a$  and bond length R. For molecular labels, see text.

10 show HB BSO values calculated from local mode force constants  $k^a$  via the generalized Badger rule, and the relationship between local mode HB force constant  $k^a$  and bond length R. The corresponding relationships between HB force constant  $k^a$  and energy density  $H_p$ , as well as between HB force constant  $k^a$  and the atomic charge difference between the two atoms engaged in the HB, are presented in Figures S1 – S3 of the Supplementary Information. In the following HBs for the Fe(III)Mb, Mn(III)Mb, and Co(III)Mb–ligand complexes are discussed, followed by the CNM analysis comparing  $\epsilon$  and  $\delta$  hydrogen bonding.

### 3.4.1 HBs in Fe(III)Mb

According to Figure 8a and Table 5, the weakest HBs for the Fe(III)Mb–ligand complexes are observed for **Fe(MET)e**, **Fe(H2O)e**, and **Fe(ONO)e** (average  $k^a$  value of 0.114 mDyn/Å) which are HBs of O···H type involving the  $\epsilon$  form of distal histidine. For **Fe(MET)e** and **Fe(H2O)e** the weak HBs are paired with weak Fe–ligand bonds (average  $k^a$  value of 0.162 mDyn/Å). That is not the case for **Fe(ONO)e**, where the ionic ONO ligand forms a strong Fe–ligand bond ( $k^a$  value of 2.020 mDyn/Å). The strongest HBs (average  $k^a$  value of 0.340 mDyn/Å) are found for **Fe(MET)d** and **Fe(H2O)d**. They are of N···H type involving the

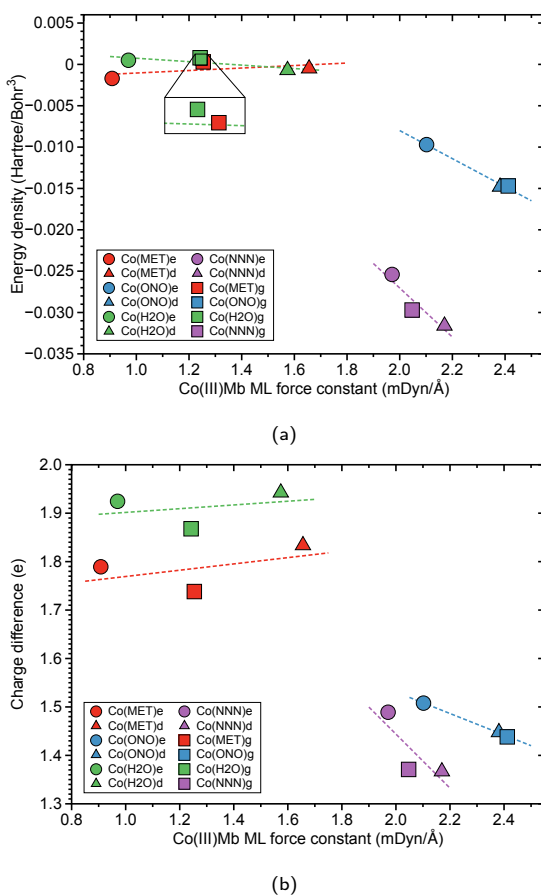


Fig. 7 Properties of ML bonds in Co(III)Mb-ligand complexes and corresponding gas phase models. a) Relation between local mode force constant  $k^a$  and energy density  $H_p$ . b) Relation between local mode force constant  $k^a$  and atomic charge difference. For molecular labels, see text.

$\delta$  form of distal histidine and are paired with only medium strong Fe-ligand bonds. The HB in **Fe(NNN)e** is relatively strong ( $k^a$  value of 0.298 mDyn/Å), paired with a relatively strong Fe-ligand bond. The findings suggest that there is no obvious correlation between the HB and the ML bond strengths. However, we observe a general trend that the N···H type HBs involving  $\delta$  histidine are stronger than O···H type HBs involving  $\epsilon$  histidine. The same is observed for the HBs in the gas phase molecular complexes, where according to Table 5, the water dimer (**H<sub>2</sub>OHOH**) with the O atom acting as a hydrogen acceptor ( $k^a$  value of 0.214 mDyn/Å) has a weaker HB weaker than the water–ammonia pair (**HOHNH<sub>3</sub>**) with the N atom acting as an acceptor ( $k^a$  value of 0.239 mDyn/Å). Interesting to note is also that the O···H type HBs of the protein are considerably weaker than the HB of the water dimer in the gas phase. In contrast, the N···H type HBs of the protein are stronger than the corresponding HB of the water–ammonia pair in the gas phase, indicating on the influence of both the transition metal and the protein environment on the HB strength.

According to the Figure S1a of the Supplementary Information, the weak O···H type HBs in **Fe(MET)e**, **Fe(H2O)e**, and **Fe(ONO)e**, exhibit on small covalent character as indicated by

Table 4 Bond length R, local mode force constant  $k^a$ , energy density at bond critical bond  $H_p$ , charge difference  $\Delta q$ , and bond strength order BSO of ML bonds in Co(III)Mb–ligand complexes along with the corresponding gas phase models investigated in our study; for molecular labels, see text

Molecule	Bond	R Å	$k^a$ mDyn/Å	$H_p$ Hr/Bohr <sup>3</sup>	$\Delta q$ e	BSO
Co(MET)e	CoO	2.020	0.908	-0.0017	1.789	0.226
Co(MET)d	CoO	1.934	1.656	-0.0005	1.834	0.457
Co(ONO)e	CoO	1.878	2.102	-0.0097	1.508	0.605
Co(ONO)d	CoO	1.856	2.381	-0.0148	1.448	0.700
Co(H2O)e	CoO	2.008	0.970	0.0005	1.924	0.244
Co(H2O)d	CoO	1.937	1.574	-0.0007	1.943	0.431
Co(NNN)e	CoN	1.914	1.971	-0.0254	1.489	0.561
Co(NNN)d	CoN	1.892	2.170	-0.0316	1.367	0.628
Co(MET)g	CoO	1.975	1.254	0.0003	1.738	0.330
Co(ONO)g	CoO	1.855	2.412	-0.0147	1.438	0.710
Co(H2O)g	CoO	1.975	1.242	0.0008	1.868	0.326
Co(NNN)g	CoN	1.902	2.047	-0.0297	1.371	0.586

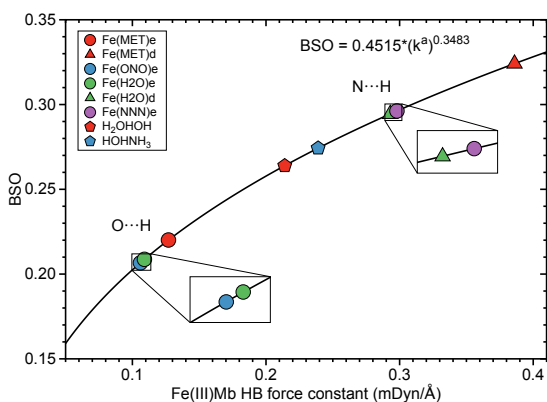
Table 5 Bond length R, local mode force constant  $k^a$ , energy density at bond critical bond  $H_p$ , charge difference  $\Delta q$ , and bond strength order BSO of protein–ligand HBs in Fe(III)Mb, Mn(III)Mb, and Co(III)Mb–ligand complexes and the water dimer and water–ammonia pair reference systems; for molecular labels, see text

Molecule	Bond	R Å	$k^a$ mDyn/Å	$H_p$ Hr/Bohr <sup>3</sup>	$\Delta q$ e	BSO
Fe(MET)e	O···H	2.074	0.127	-0.0008	1.223	0.220
Fe(MET)d	N···H	1.620	0.386	-0.0118	1.111	0.324
Fe(ONO)e	O···H	2.195	0.106	-0.0006	0.994	0.207
Fe(H2O)e	O···H	2.094	0.109	-0.0006	1.421	0.209
Fe(H2O)d	N···H	1.726	0.293	-0.0037	1.103	0.294
Fe(NNN)e	N···H	1.850	0.298	-0.0011	1.018	0.296
Mn(MET)e	O···H	2.174	0.114	-0.0004	1.235	0.212
Mn(MET)d	N···H	1.559	0.346	-0.0210	1.117	0.312
Mn(ONO)e	O···H	1.952	0.180	-0.0014	1.091	0.248
Mn(H2O)e	O···H	2.134	0.081	-0.0004	1.421	0.188
Mn(H2O)d	N···H	1.743	0.251	-0.0035	1.112	0.279
Mn(NNN)e	N···H	1.744	0.356	-0.0033	1.123	0.315
Co(MET)e	O···H	2.169	0.141	-0.0004	1.170	0.228
Co(MET)d	N···H	1.605	0.343	-0.0141	1.121	0.311
Co(ONO)e	O···H	2.159	0.118	-0.0007	0.962	0.215
Co(H2O)e	O···H	2.251	0.051	0.0001	1.346	0.160
Co(H2O)d	N···H	1.684	0.280	-0.0063	1.114	0.290
Co(NNN)e	N···H	1.827	0.312	-0.0014	0.993	0.301
H <sub>2</sub> OHOH	O···H	1.906	0.214	-0.0013	1.446	0.264
HOHNH <sub>3</sub>	N···H	1.917	0.239	-0.0016	1.657	0.274

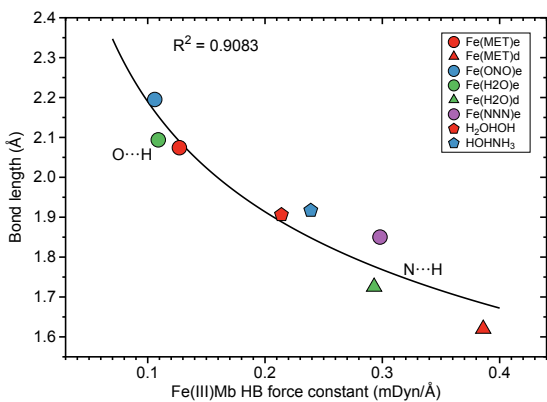
their small negative energy density values. On the other hand, the strong N···H type HBs of **Fe(MET)d** and **Fe(H2O)d**, have more negative energy density values, disclosing more covalent bond character. It is interesting to note that the covalent character of the gas phase reference molecules (**H<sub>2</sub>OHOH** and **HOHNH<sub>3</sub>**), is relatively small, which indicates on a predominant effect of the protein environment, increasing the covalent character of the N···H type HBs and their strength. According to Figure 8b, the HB bond strength of the Fe(III)Mb proteins shows a weak correlation with the corresponding HB bond length, with the N···H bonds being overall shorter than their O···H counterparts.

### 3.4.2 HBs in Mn(III)Mb

HB BSOs as a function of the corresponding local mode force constants  $k^a$ s, calculated from the extended Badger relationship (see above), as well the correlation between HB force constants  $k^a$  and HB bond length R, for the Mn(III)Mb – ligand complexes are

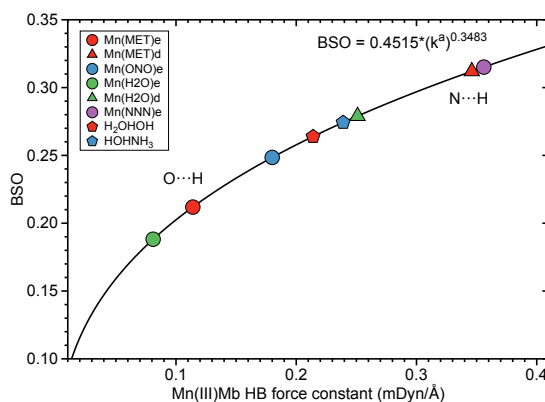


(a)

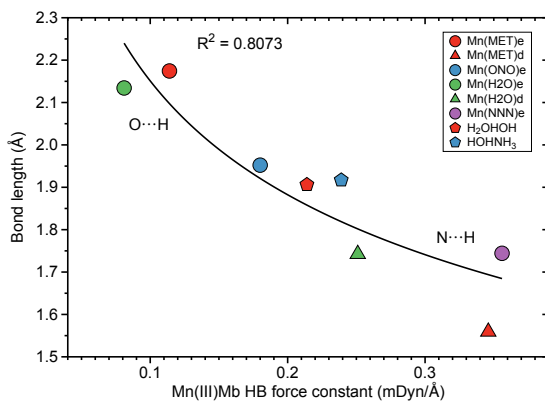


(b)

Fig. 8 HB properties of Fe(III)Mb-ligand complexes and corresponding properties of the water and water-ammonia molecular complexes. a) Bond strength order BSO calculated from local mode force constants  $k^a$  via the generalized Badger rule. b) Relation between local mode force constant  $k^a$  and bond length R. For molecular labels, see text.



(a)



(b)

Fig. 9 HB properties of Mn(III)Mb-ligand complexes and corresponding properties of the water and water-ammonia molecular complexes. a) Bond strength order BSO calculated from local mode force constants  $k^a$  via the generalized Badger rule. b) Relation between local mode force constant  $k^a$  and bond length R. For molecular labels, see text.

shown in Figures 9a and 9b. The correlation between HB force constant  $k^a$  and energy density  $H_p$ , as well as the correlation between  $k^a$  and charge difference between the two atoms involved in HB are presented in Figure S2 of the Supplementary Information.

Overall we observe the same trends as for the Fe(III)Mb-ligand complexes with the following exceptions. As shown in Figure 9a, weak O···H type HBs are formed between the neutral ligands and the  $\epsilon$  form of distal histidine, namely **Mn(MET)e** and **Mn(H2O)e**. We find the strongest N···H type HB for the  $\epsilon$  form of distal histidine with the azide anion (**Mn(NNN)e**). The strongest HBs of N···H type involving the  $\delta$  form of distal histidine are found for **Mn(MET)d** and **Mn(H2O)d**. Whereas similar to Fe(III)Mb, the weaker O···H type HB of textbf{Mn(H2O)e} is paired with a weaker Mn-ligand bond for the  $\epsilon$  Mn(III)Mb protein, for **Mn(ONO)e** and **Mn(MET)e** the Mn-ligand bond strength lies in the middle range. The  $\epsilon$  form of the Mn(III)Mb protein azide complex (**Mn(NNN)e**) with the strongest N···H type HB in this series is paired with a Mn-ligand bond of middle strength.

### 3.4.3 HBs in Co(III)Mb

Figures 10a and 10b present BSO values as a function of the local mode HB force constants  $k^a$  for the Co(III)Mb-ligand complexes, calculated from the extended Badger relationship, and the correlation between the HB force constants  $k^a$  and the corresponding bond length R. In addition, Figure S3 of Supplementary Information presents the correlation between HB force constant  $k^a$  and energy density  $H_p$ , as well the correlation between  $k^a$  and the charge difference between the two atoms involved in the HB.

Generally, for the Co(III)Mb-ligand complexes we observe the same trends as for the Fe(III)Mb-ligand systems with some exceptions. According to Figure 10a, the weakest HBs of the O···H type are found for the  $\epsilon$  form of the Co(III)Mb protein (**Co(MET)e**, **Co(ONO)e**, and **Co(H2O)e**). The HB of the N···H type for the same  $\epsilon$  protein system (**Co(NNN)e**), is one of the strongest HB in this series. Moreover, both  $\delta$  Co(III)Mb proteins (**Co(MET)d** and **Co(H2O)d**) form relatively strong HBs of the N···H type. Similarly as in the Fe(III)Mb and Mn(III)Mb protein systems, the weaker Co-ligand chemical bonds in the **Co(MET)e** and **Co(H2O)e** are paired with the weaker HBs of the O···H type, however for the azide anion **Co(NNN)e**, both a strong Co-ligand

bond and a strong N···H type HB are observed.

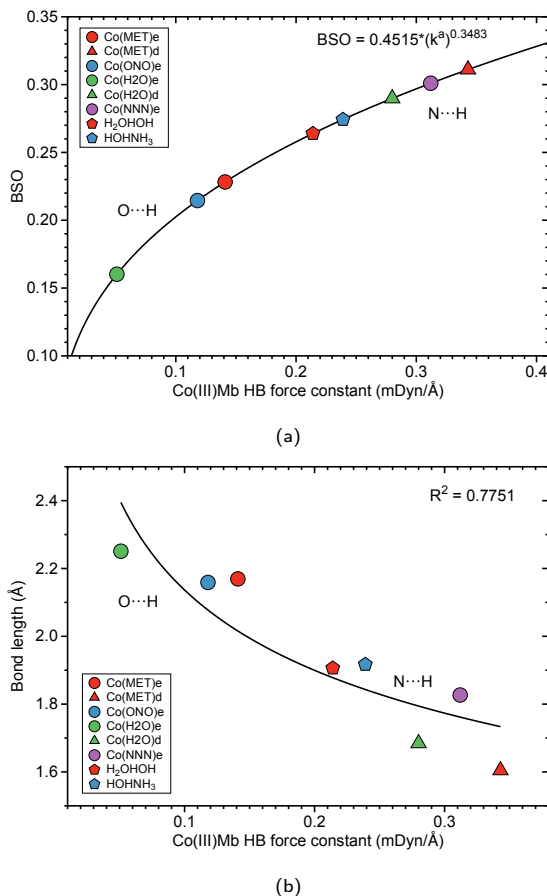


Fig. 10 HB properties of CO(III)Mb-ligand complexes and corresponding properties of the water and water-ammonia molecular complexes. a) Relationship between local mode force constant  $k^a$  and BSO. b) Relation between local mode force constant  $k^a$  and bond length  $R$ . For molecular labels, see text.

### 3.5 $\varepsilon$ versus $\delta$ HB visualized by CNM

Additional insights into the difference between  $\varepsilon$  versus  $\delta$  ligand-histidine HB determining e.g., the orientation of small molecular ligands in the heme pocket can be gained via our CNM analysis, which decomposes the normal vibrational modes of a molecule into local mode parameters, and as such can identify how the atoms of a specific structural element or functional group move during a specific vibration.<sup>49,50</sup> However, it has to be noted that whereas LMA properties can be calculated for a restricted number of local mode parameters of interest, such as the HB force constants  $k^a(\text{HB})$  and the ML bond constants  $k^a(\text{ML})$  as in this work, CNM requires the proper choice of a chemically meaningful complete and non-redundant set of  $N_{\text{vib}}$  local mode parameters, with  $N_{\text{vib}} = (3N - 6)$  for a non-linear and  $(3N - 5)$  for a linear molecule being composed of N atoms. This can become unfeasible for systems with a large number of atoms ( $N > 100$ ), such as QM/MM systems, where  $N_{\text{vib}}$  is determined from the total number of QM and MM atoms, when performed manually or starting from a large redundant coordinate set and applying some trial and er-

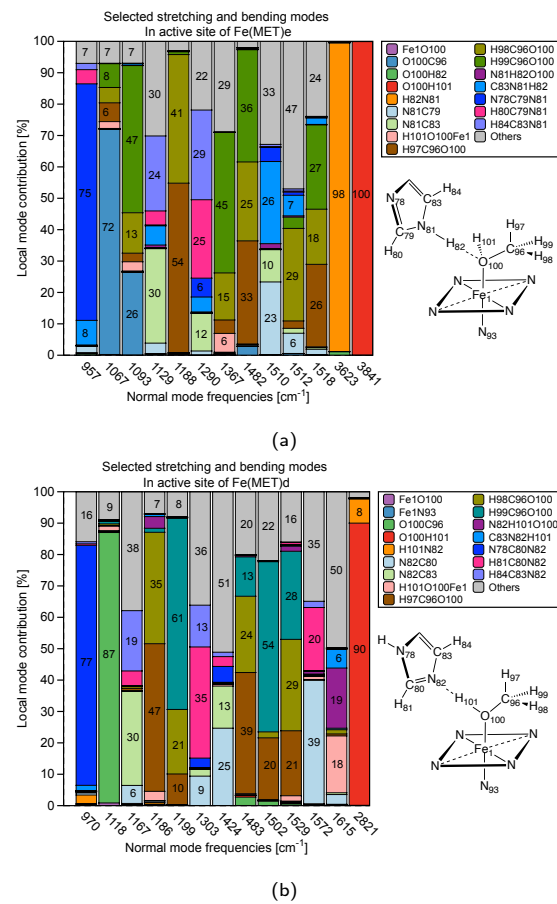


Fig. 11 Decomposition of normal vibrational modes into local stretching and bending contributions involved in O···H type and N···H type HB. a) Fe(MET)e as representative for O···H type HB; b) Fe(MET)d as representative for N···H type HB. For molecular labels, see text.

ror procedures. Our group has developed two methods in order to help in this situation; i) the generalized subsystem vibrational analysis (GSVA) developed in our group<sup>108,109</sup> which projects out from the full  $N_{\text{vib}}$  QM/MM set the important QM vibrations and ii) LModeAGen<sup>67</sup> which offers a convenient way for the generation of local mode parameters based on chemical graph theory.<sup>110</sup>

In the following the CNM analysis for the Fe(MET)e and Fe(MET)d complexes is discussed as an example. Both complexes contain 3049 atoms (103 QM atoms, 2946 MM atoms) leading to a total of  $N_{\text{vib}} = 9141$ . After the GSVA procedure extracting the 297 QM normal modes of interest, LModeAGen was applied to generated a set of local mode parameters. In Figures 11a and 11b the CNM is shown in the range of 900 - 3000 cm<sup>-1</sup> focusing on the different role of the MET OH bond. Figure 11a shows the CNM for Fe(MET)e where one of the distal histidine N-H bonds serves as HB donor and the MET oxygen as HB acceptor, whereas the MET OH bond is a spectator bond. Figure 11b shows the CNM for Fe(MET)d where the distal histidine nitrogen atom serves as HB acceptor and MET OH bond as HB donor.

Figure 11a clearly confirms the spectator character of the OH MET bond in Fe(MET)e; the normal mode representing the OH MET stretching vibration has 100 % local OH stretching mode

character, in line with the  $3841\text{ cm}^{-1}$  OH stretching frequency, which is in the normal OH stretching range.<sup>111</sup> The NH bond of histidine serving as HB donor is with a frequency value of  $3623\text{ cm}^{-1}$  some slightly redshifted<sup>111</sup>, but also has 98 % local NH mode character. A different picture emerges for **Fe(MET)d** as revealed by the CNM shown in Figure 11b. The OH MET bond of **Fe(MET)d** serves as HB donor. As a consequence, the OH stretching frequency is considerably redshifted ( $2821\text{ cm}^{-1}$ ). It has 90 % local OH stretching character with an 8 % admixture of N···H local mode stretching; elucidating the different scenarios of OH MET bonding; qualifying CNM as a helpful tool for artificial Mb designers.

#### 4 Conclusions and outlook

Based on comprehensive QM/MM calculations combined with LMA, we investigated the strength of ML bonding with methanol, water, nitrite, and azide as model ligands in the active site of Fe(III)Mb, Mn(III)Mb, and Co(III)Mb. This analysis was conducted for both the  $\epsilon$  and  $\delta$  forms of the distal histidine. In addition to ML bonding, we explored potential HB between the ligand and the distal histidine, a possibility that has not received much attention to date. To account for the effects of the protein environment, we also examined the corresponding gas-phase models of the protein active sites, using the same metals and ligands. HBs in the protein were compared with HBs in the water and water–ammonia molecular complexes.

As depicted in Figure 12a the results of our study show that the two neutral ligands methanol and water form relatively weak ML bonds compared to their ionic counterparts nitrite and azide, forming considerably stronger ML bonds. Moreover, ML bonds are weaker in the protein than in the gas phase models, which indicates that the protein environment influences ML bond formation/cleavage. The strength of the ML protein bonds also depends on the protonation form of the distal histidine, namely for the  $\epsilon$  form of this residue the ML bond is generally weaker than that for the  $\delta$  form (see Figure 12a).

Overall, the average strength of the Co-ligand bonds (average  $k^a$  of  $1.724\text{ mDyn}/\text{\AA}$ ) is greater than the average strength of Fe-ligand bonds (average  $k^a$  of  $1.415\text{ mDyn}/\text{\AA}$ ) and that of Mn-ligand bonds ( $k^a$  of  $0.882\text{ mDyn}/\text{\AA}$ ). These findings provide useful guidelines for fine-tuning of artificial Mbs with specific ML bond strengths. According to Figure 12b summarizing the strength of the ML bonds for all three metals, the strength of the ML bonds with Fe covers a broader range than the other metals, which indicates that Fe should be selected as a candidate for a catalyst in chemical reactions that require ML bonds of different strengths.

For the  $\epsilon$  histidine tautomer (see Figure 13a) most ligands form O···H type HBs, where the distal histidine is the hydrogen atom donor, while for the  $\delta$  tautomer N···H type HBs are formed with the distal histidine as HB acceptor. According to our calculations, the N···H type HBs are stronger and shorter in the proteins than in the reference water–ammonia pair, moving the ligands closer to the metal. However, as revealed by Figure 13b we did not observe a direct correlation between ML and HB bond strengths.

The analysis of the HBs formed between the ligands and the distal histidine of Mb adds another layer of useful information,

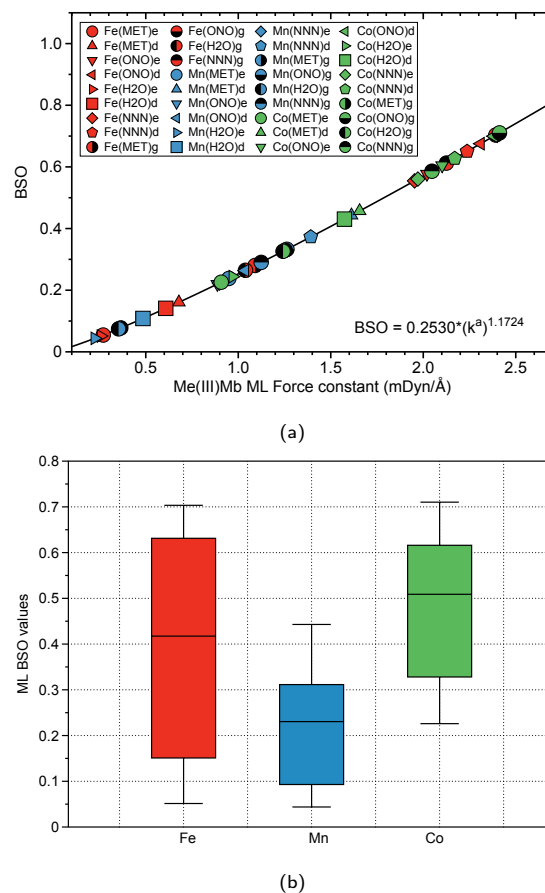


Fig. 12 a) Bond strength order BSO calculated from local mode force constants  $k^a$  via the generalized Badger rule for all ML bonds of MB complexes and gas phase models investigated in this study (Me = Fe, Mn, and Co). For molecular labels, see text. b) Box and whisker plot of BSO values for all ML bonds investigated in this study.

such as on the strength and covalency of HBs formed between ligand and histidine, with O···H type HBs overall weaker than their N···H type HB counterparts (see Figure 13aa and how these HBs may influence the ligand orientation in the Mb pocket). We confirmed that stronger HBs are formed with the ionic ligands (nitrite and azide) compared to the neutral ones (methanol and water), which can be useful for the design of ionic reactants and intermediates of catalytic reactions taking place in the active site of Mb and/or its mutations.

A recent experimental investigation shows that replacing the native Mb porphine ring with a porphycene ring increases the protein's catalytic activity for the dehydration of various aldehydes.<sup>112</sup> These authors suggest that this enhancement is attributed to the involvement of the distal histidine in the reaction, and that a HB with the distal histidine determines the ligand's correct orientation, significantly reducing the reaction's activation energy. Furthermore, they propose that the hydrogen atom of histidine involved in the HB directly participates in the reaction, underscoring the crucial role of this HB in the overall reaction mechanism. We are currently exploring the mechanistic details with our Unified Reaction Valley Approach (URVA)<sup>113,114</sup> combined with LMA, which will provide a comprehensive, holistic

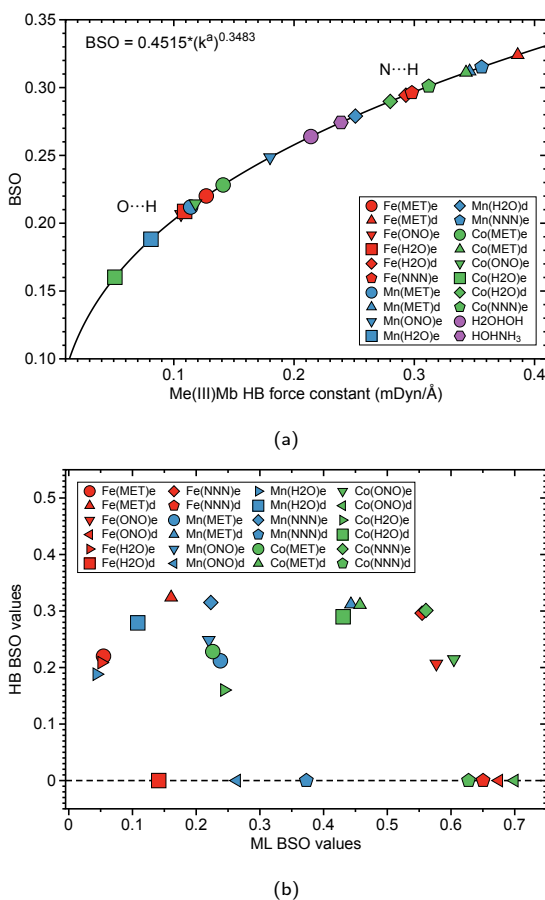


Fig. 13 a) Bond strength order BSO calculated from local mode force constants  $k^a$  via the generalized Badger rule for all HB bonds of MB complexes investigated in this study (Me = Fe, Mn, and Co). b) Relation between ML and HB bond strengths for all MB complexes investigated in this study. Zero HB BSO values indicate the lack of HB opportunity. For molecular labels, see text.

picture. The results will be published in a forthcoming article.

In conclusion, our investigation provides in-depth insight into the strength of ML bonds formed between four prototype ligands (methanol, water, nitrite, and azide) and the metal centers in Fe, Mn, and Co myoglobins at the atomic level. As illustrated in the box-and-whisker plot in Figure 12b, Fe exhibits a broader variation in ML bond strengths compared to Mn and Co. This suggests that Fe, the metal found in native myoglobin, is the most versatile candidate for designing artificial myoglobins for catalytic applications that require variable ML bond strengths. However, Mn, Co or other metals might still be preferable for specific synthetic reasons or in cases, such as PET-RAFT polymerization, where specific excitation of the metal is needed. Additionally, as shown in our study, analyzing potential HB interactions between ligands and the distal Mb histidine provides valuable insights into how small molecular ligands orient within the heme pocket. As revealed by our results this orientation is guided by the strength of the HBs formed with the distal histidine.

Overall, our findings identify the strength of both ML bonds and HBs, fully captured by LMA, as a key parameter determin-

ing the catalytic activity and function of Mbs. This is particularly relevant when considering neutral versus ionic ligands and other metals such as Mn or Co as alternatives to Fe. The insights gained through our investigation offer valuable guidance for strategically fine-tuning existing artificial Mbs and designing new, versatile variants. Specifically, bond strength combinations like those illustrated in Figure 13b provide a practical roadmap for future exploration. We hope that our QM/MM-LMA protocol will become a valuable addition to the research community's toolkit.

## Author contributions

Marek Freindorf (<https://orcid.org/0000-0001-5285-5455>): writing - review and editing, conceptualization, investigation, data curation, methodology; Elfi Kraka (<https://orcid.org/0000-0002-9658-5626>): writing - review and editing, conceptualization, funding acquisition, supervision.

## Conflicts of interest

There are no conflicts to declare.

## Data availability

The data supporting this article have been included as part of the Supplementary Information.

## Acknowledgements

We thank the SMU O'Donnell Data Science and Research Computing Institute for providing generous computational resources. This work was financially supported by the National Science Foundation, Grant CHE 2102461. We also thank Bangaru Bhaskararao and Juliana Antonio for fruitful discussions.

## Notes and references

- 1 B. M. Hoffman, *The Porphyrins*, Academic Press, New York, 1979, vol. 7, pp. 403–444.
- 2 J. S. Olson, *Antioxid. Redox Sign.*, 2019, **32**, 228–246.
- 3 G. A. Ordway and D. J. Garry, *J. Exp. Biol.*, 2004, **207**, 3441–3446.
- 4 I. E. Elkholi, M. E. Elsherbiny and M. Emara, *Biochim. Biophys. Acta*, 2022, **1877**, 188706.
- 5 E. Zonetff, Y. Wang, C. Jackson, O. Smith, S. Duchi, C. Onofrillo, B. Farrugia, S. Moulton, R. Williams, C. Parish, D. R. Nisbet and L. M. Caballero-Aguilar, *Nat. Commun.*, 2024, **15**, 4361.
- 6 F. Darain, P. Yager, K. L. Gan and S. C. Tjin, *Biosens. Bioelectron.*, 2009, **24**, 1744–1750.
- 7 K. K. Adepu, A. Anishkin, S. H. Adams and S. V. Chintapalli, *Physiol. Rev.*, 2024, **104**, 1611–1642.
- 8 Y. Kagawa, K. Oohora and T. Hayashi, *J. Inorg. Biochem.*, 2024, **252**, 112459.
- 9 K. Oohora, A. Onoda and T. Hayashi, *Acc. Chem. Res.*, 2019, **52**, 945–954.
- 10 M. Tinzl, J. V. Diedrich, P. R. Mittl, M. Clémancey, M. Reiher, J. Proppe, J.-M. Latour and D. Hilvert, *J. Am. Chem. Soc.*, 2024, **146**, 1957–1966.

11 K. Yu and T. R. Ward, *J. Inorg. Bioch.*, 2024, **258**, 112621.1–18.

12 W.-N. Xu, Y.-D. Gao, P. Su, L. Huang, Z.-L. He and L.-C. Yang, *ACS Catalysis*, 2024, **14**, 14139–14160.

13 Y.-W. Lin, *J. Inorg. Biochem.*, 2024, **257**, 112595.1–14.

14 M. Bordeaux, V. Tyagi and R. Fasan, *Angew. Chem. Int. Ed.*, 2015, **127**, 1764–1768.

15 H. M. Key, P. Dydio, D. S. Clark and J. F. Hartwig, *Nature*, 2016, **534**, 534–537.

16 P. Dydio, H. M. Key, A. Nazarenko, J. Y.-E. Rha, V. Seyed-kazemi, D. S. Clark and J. F. Hartwig, *Science*, 2016, **354**, 102–106.

17 G. Sreenilayam, E. J. Moore, V. Steck and R. Fasan, *Adv. Synth. Cat.*, 2017, **359**, 2076–2089.

18 Z. N. Zahran, L. Chooback, D. M. Copeland, A. H. West and G. B. Richter-Addo, *J. Inorg. Biochem.*, 2008, **102**, 216–233.

19 K. L. Stone and S. M. Ahmed, *Inorganics*, 2016, **4**, e12.1–e12.16.

20 R. Lin, C. E. Immoos and P. J. Farmer, *J. Biol. Inorg. Chem.*, 2000, **5**, 738–747.

21 K. Oohora, Y. Kihira, E. Mizohata, T. Inoue and T. Hayashi, *J. Am. Chem. Soc.*, 2013, **135**, 17282–17285.

22 K. Oohora, H. Meichin, Y. Kihira, H. Sugimoto, Y. Shiro and T. Hayashi, *J. Am. Chem. Soc.*, 2017, **139**, 18460–18463.

23 K. L. Stone, J. Hua and H. Choudhry, *Inorganics*, 2015, **3**, 219–229.

24 T. M. Makris, K. v. Koenig, I. Schlichting and S. G. Sligar, *J. Inorg. Biochem.*, 2006, **100**, 507–518.

25 H. Hirao, K.-B. Cho and S. Shaik, *J. Biol. Inorg. Chem.*, 2008, **13**, 521–530.

26 S.-C. Chien, O. Shoji, Y. Morimoto and Y. Watanabe, *New J. Chem.*, 2017, **41**, 302–307.

27 N. Kawakami, O. Shoji and Y. Watanabe, *ChemBioChem*, 2012, **13**, 2045–2047.

28 K. Omura, Y. Aiba, H. Onoda, J. K. Stanfield, S. Ariyasu, H. Sugimoto, Y. Shiro, O. Shoji and Y. Watanabe, *Chem. Comm.*, 2018, **54**, 7892–7895.

29 K. Omura, Y. Aiba, K. Suzuki, S. Ariyasu, H. Sugimoto and O. Shoji, *ACS Cat.*, 2022, **12**, 11108–11117.

30 S. I. Mann, A. Nayak, G. T. Gassner, M. J. Therien and W. F. DeGrado, *J. Am. Chem. Soc.*, 2021, **143**, 252–259.

31 I. Degtyarenko, R. M. Nieminen and C. Rovira, *Biophys. J.*, 2006, **91**, 2024–2034.

32 S. Neya, M. Suzuki, T. Hoshino and A. T. Kawaguchi, *Inorg. Chem.*, 2013, **52**, 7387–7393.

33 T. D. Rapson, S. Warneke, M. M. Musameh, H. Dacres, B. C. T. Macdonald and S. C. Trowell, *RSC Adv.*, 2015, **5**, 89003–89008.

34 Y. Morita, K. Oohora, E. Mizohata, A. Sawada, T. Kamachi, K. Yoshizawa, T. Inoue and T. Hayashi, *Inorg. Chem.*, 2016, **55**, 1287–1295.

35 A. T. Smith, T. Majtan, K. M. Freeman, Y. Su, J. P. Kraus and J. N. Burstyn, *Inorg. Chem.*, 2011, **50**, 4417–4427.

36 J. G. Kleingardner, B. Kandemir and K. L. Bren, *J. Am. Chem. Soc.*, 2014, **136**, 4–7.

37 D. J. Sommer, M. D. Vaughn, B. C. Clark, J. Tomlin, A. Roy and G. Ghirlanda, *Biochim. Biophys. Acta*, 2016, **1857**, 598–603.

38 K. Kitanishi, M. Shimonaka and M. Unno, *ACS Omega*, 2021, **6**, 34912–34919.

39 L. J. Perkins, B. R. Weaver, A. R. Buller and J. N. Burstyn, *Proc. Nat. Acad. Sci.*, 2021, **118**, e2017625118.

40 M. Meglioli, G. Di Rocco, A. Ranieri, C. A. Bortolotti, M. Sola, G. Battistuzzi and M. Borsari, *ChemElectroChem*, 2024, **11**, e202300821.

41 V. Firpo, J. M. Le, V. Pavone, A. Lombardi and K. L. Bren, *Chemical Science*, 2018, **9**, 8582–8589.

42 R. J. Labidi, B. Faivre, P. Carpentier, J. Perard, P. Gotico, Y. Li, M. Atta and M. Fontecave, *J. Am. Chem. Soc.*, 2024, **146**, 28296–28305.

43 I. C. Anderson, D. C. Gomez, M. Zhang, S. J. Koehler and C. A. Figg, *Angew. Chem. Int. Ed.*, 2024, **n/a**, e202414431.

44 C. E. Tzelioiu, M. A. Mermigki and D. Tzeli, *Molecules*, 2022, **27**, 2660.

45 M. W. van der Kamp and A. J. Mulholland, *Biochemistry*, 2013, **52**, 2708–2728.

46 V. Guallar and F. H. Wallrapp, *Biophys. Chem.*, 2010, **149**, 1–11.

47 A. Warshel and M. Levitt, *J. Mol. Biol.*, 1976, **103**, 227–249.

48 A. Warshel and M. Karplus, *J. Am. Chem. Soc.*, 1972, **94**, 5612–5625.

49 E. Kraka, W. Zou and Y. Tao, *WIREs: Comput. Mol. Sci.*, 2020, **10**, 1480.

50 E. Kraka, M. Quintano, H. W. La Force, J. J. Antonio and M. Freindorf, *J. Phys. Chem. A*, 2022, **126**, 8781–8798.

51 R. F. W. Bader, *Monatshefte für Chemie*, 2005, **136**, 819–854.

52 R. F. W. Bader, *Atoms in Molecules: A Quantum Theory (International Series of Monographs on Chemistry)*, Clarendon Press, 1994.

53 R. F. W. Bader, *Chem. Rev.*, 1991, **91**, 893–928.

54 A. E. Reed, L. A. Curtiss and F. Weinhold, *Chem. Rev.*, 1988, **88**, 899–926.

55 F. Weinhold and C. R. Landis, *Valency and Bonding: A Natural Bond Orbital Donor-Acceptor Perspective*, Cambridge University Press, 2005.

56 J. D. Kelley and J. J. Leventhal, in *Problems in Classical and Quantum Mechanics: Normal Modes and Coordinates*, Springer, 2017, pp. 95–117.

57 E. Wilson, J. Decius and P. Cross, *Molecular Vibrations. The Theory of Infrared and Raman Vibrational Spectra*, McGraw-Hill, New York, 1955.

58 Z. Konkoli and D. Cremer, *Int. J. Quantum Chem.*, 1998, **67**, 1–9.

59 Z. Konkoli, J. A. Larsson and D. Cremer, *Int. J. Quantum Chem.*, 1998, **67**, 11–27.

60 E. B. Wilson, *J. Chem. Phys.*, 1941, **9**, 76–84.

61 E. Wilson, J. Decius and P. Cross, *Molecular Vibrations. The*

*Theory of Infrared and Raman Vibrational Spectra*, McGraw-Hill, New York, 1955.

62 V. Barone, S. Alessandrini, M. Biczysko, J. R. Cheeseman, D. C. Clary, A. B. McCoy, R. J. DiRisio, F. Neese, M. Melosso and C. Puzzarini, *Nat. Rev. Met. Prim.*, 2021, **1**, 38.

63 W. Zou and D. Cremer, *Theor. Chem. Acc.*, 2014, **133**, 1451–1466.

64 M. Freindorf and E. Kraka, *J. Mol. Model.*, 2020, **26**, 281–1–281–15.

65 M. Freindorf, A. A. A. Delgado and E. Kraka, *J. Comp. Chem.*, 2022, **43**, 1725–1746.

66 A. Madushanka, N. Verma, M. Freindorf and E. Kraka, *Int. J. Mol. Sci.*, 2022, **23**, 12310–1–12310–25.

67 R. T. Moura, Jr., M. Quintano, J. J. Antonio, M. Freindorf and E. Kraka, *J. Phys. Chem. A*, 2022, **126**, 9313–9331.

68 J. J. Antonio and E. Kraka, *Biochemistry*, 2023, **62**, 2325–2337.

69 M. Freindorf, J. Antonio and E. Kraka, *J. Phys. Chem. A*, 2023, **127**, 8316–8329.

70 M. Freindorf, J. Antonio and E. Kraka, *J. Comput. Chem.*, 2024, **45**, 574–588.

71 Y. Dangat, M. Freindorf and E. Kraka, *J. Am. Chem. Soc.*, 2024, **146**, 145–158.

72 Z. Konkoli and D. Cremer, *Int. J. Quantum Chem.*, 1998, **67**, 29–40.

73 Z. Konkoli, J. A. Larsson and D. Cremer, *Int. J. Quantum Chem.*, 1998, **67**, 41–55.

74 N. Verma, Y. Tao, W. Zou, X. Chen, X. Chen, M. Freindorf and E. Kraka, *Sensors*, 2020, **20**, 2358.

75 M. Quintano, A. A. A. Delgado, R. T. Moura Jr, M. Freindorf and E. Kraka, *Electron. Struct.*, 2022, **4**, 044005–1–044005–17.

76 M. Quintano, R. T. Moura Jr. and E. Kraka, *Chem. Phys. Lett.*, 2024, **849**, 141416–1141416–13.

77 W. Zou and D. Cremer, *Chem. Eur. J.*, 2016, **22**, 4087–4099.

78 D. Cremer and E. Kraka, *Curr. Org. Chem.*, 2010, **14**, 1524–1560.

79 E. Kraka, J. A. Larsson and D. Cremer, *Computational Spectroscopy*, Wiley, New York, 2010, pp. 105–149.

80 I. Mayer, *Chem. Phys. Lett.*, 1983, **97**, 270–274.

81 I. Mayer, *Int. J. Quantum Chem.*, 1986, **29**, 477–483.

82 I. Mayer, *J. Comput. Chem.*, 2007, **28**, 204–221.

83 E. Kraka and M. Freindorf, *Reference Module in Chemistry, Molecular Sciences and Chemical Engineering - Comprehensive Computational Chemistry*, Elsevier, Heidelberg, 2022, pp. 1–27.

84 D. Cremer and E. Kraka, *Angew. Chem. Int. Ed.*, 1984, **23**, 627–628.

85 D. Cremer and E. Kraka, *Croatica Chem. Acta*, 1984, **57**, 1259–1281.

86 F. Weinhold, C. R. Landis and E. D. Glendening, *Int. Rev. Phys. Chem.*, 2016, **35**, 399–440.

87 D. A. Case, I. Y. Ben-Shalom, S. R. Brozell, D. S. Cerutti, T. E. Cheatham, V. W. D. Cruzeiro, T. A. Darden, R. E. Duke, D. Ghoreishi, M. K. Gilson, H. Gohlke, A. W. Goetz, D. Greene, R. Harris, N. Homeyer, S. Izadi, A. Kovalenko, T. Kurtzman, T. S. Lee, S. LeGrand, P. Li, C. Lin, J. Liu, T. Luchko, R. Luo, D. J. Mermelstein, K. M. Merz, Y. Miao, G. Monard, C. Nguyen, H. Nguyen, I. Omelyan, A. Onufriev, F. Pan, R. Qi, D. R. Roe, A. Roitberg, C. Sagui, S. Schott-Verdugo, J. Shen, C. L. Simmerling, J. Smith, R. Salomon-Ferrer, J. Swails, R. C. Walker, J. Wang, H. Wei, R. M. Wolf, X. Wu, L. Xiao, D. M. York and P. A. Kollman, *AMBER*, University of California, San Francisco, 2018.

88 W. L. Jorgensen, J. Chandrasekhar, J. D. Madura, R. W. Impey and M. L. Klein, *J. Chem. Phys.*, 1983, **79**, 926–935.

89 M. Ernzerhof and J. P. Perdew, *J. Chem. Phys.*, 1998, **109**, 3313–3320.

90 J. P. Perdew, K. Burke and M. Ernzerhof, *Phys. Rev. Lett.*, 1996, **77**, 3865–3868.

91 C. Adamo and V. Barone, *J. Chem. Phys.*, 1999, **110**, 6158–6170.

92 S. Zhao, Z.-H. Li, W.-N. Wang, Z.-P. Liu, K.-N. Fan, Y. Xie and H. F. Schaefer, *J. Chem. Phys.*, 2006, **124**, 184102.

93 C. J. Cramer and D. G. Truhlar, *Phys. Chem. Chem. Phys.*, 2009, **11**, 10757–10816.

94 S. Li, J. M. Hennigan, D. A. Dixon and K. A. Peterson, *J. Phys. Chem. A*, 2009, **113**, 7861–7877.

95 R. Ditchfield, W. J. Hehre and J. A. Pople, *J. Chem. Phys.*, 1971, **54**, 724–728.

96 L. W. Chung, W. M. C. Sameera, R. Ramozzi, A. J. Page, M. Hatanaka, G. P. Petrova, T. V. Harris, X. Li, Z. Ke, F. Liu, H.-B. Li, L. Ding and K. Morokuma, *Chem. Rev.*, 2015, **115**, 5678–5796.

97 M. K. Safo, G. P. Gupta, F. A. Walker and W. R. Scheidt, *J. Am. Chem. Soc.*, 1991, **113**, 5497–5510.

98 G. McLendon and K. Sandberg, *J. Biol. Chem.*, 1978, **253**, 3913–3917.

99 S. Della Longa, S. Pin, R. Cortès, A. V. Soldatov and B. Alpert, *Biophys. J.*, 1998, **75**, 3154–3162.

100 T. Harami, *J. Phys. Chem.*, 1979, **71**, 1309–1318.

101 R. Silaghi-Dumitrescu, D. A. Svistunenko, D. Cioloboc, C. Bischin, F. Scurtu and C. E. Cooper, *Nitric Oxide*, 2014, **42**, 32–39.

102 M. Sundararajan and F. Neese, *Inorg. Chem.*, 2015, **54**, 7209–7217.

103 R. Langley, P. Hambright, K. Alston and P. Neta, *Inorg. Chem.*, 1986, **25**, 114–117.

104 M. J. Frisch, G. W. Trucks, H. B. Schlegel, G. E. Scuseria, M. A. Robb, J. R. Cheeseman, G. Scalmani, V. Barone, G. A. Petersson, H. Nakatsuji, X. Li, M. Caricato, A. V. Marenich, J. Bloino, B. G. Janesko, R. Gomperts, B. Mennucci, H. P. Hratchian, J. V. Ortiz, A. F. Izmaylov, J. L. Sonnenberg, D. Williams-Young, F. Ding, F. Lippiani, F. Egidi, J. Goings, B. Peng, A. Petrone, T. Henderson, D. Ranasinghe, V. G. Zákrzewski, J. Gao, N. Rega, G. Zheng, W. Liang, M. Hada, M. Ehara, K. Toyota, R. Fukuda, J. Hasegawa, M. Ishida, T. Nakajima, Y. Honda, O. Kitao, H. Nakai, T. Vreven,

K. Throssell, J. A. Montgomery Jr, J. E. Peralta, F. Ogliaro, M. J. Bearpark, J. J. Heyd, E. N. Brothers, K. N. Kudin, V. N. Staroverov, T. A. Keith, R. Kobayashi, J. Normand, K. Raghavachari, A. P. Rendell, J. C. Burant, S. S. Iyengar, J. Tomasi, M. Cossi, J. M. Millam, M. Klene, C. Adamo, R. Cammi, J. W. Ochterski, R. L. Martin, K. Morokuma, O. Farkas, J. B. Foresman and D. J. Fox, *Gaussian 16*, Gaussian Inc. Wallingford CT, 2016.

105 W. Zou, R. Moura Jr, M. Quintano, F. Bodo, Y. Tao, M. Freindorf, M. Z. Makoś, N. Verma, D. Cremer and E. Kraka, *LModeA2023*, Computational and Theoretical Chemistry Group (CATCO), Southern Methodist University: Dallas, TX, USA, 2023.

106 T. A. Keith, *AIMALL*, TK Gristmill Software, Overland Park KS, 2017.

107 R. M. Badger, *J. Chem. Phys.*, 1934, **2**, 128–131.

108 Y. Tao, C. Tian, N. Verma, W. Zou, C. Wang, D. Cremer and E. Kraka, *J. Chem. Theory Comput.*, 2018, **14**, 2558–2569.

109 Y. Tao, W. Zou, S. Nanayakkara, M. Freindorf and E. Kraka, *Theor. Chem. Acc.*, 2021, **140**, 31–1–31–5.

110 M. Randić, M. Novič and D. Plavšić, *Solved and Unsolved Problems of Structural Chemistry*, CRC Press Boca Raton, 2016.

111 M. Freindorf, E. Kraka and D. Cremer, *Int. J. Quantum Chem.*, 2012, **112**, 3174–3187.

112 S. Kato, M. Abe, H. Gröger and T. Hayashi, *ACS Catalysis*, 2024, **14**, 13081–13087.

113 E. Kraka, J. J. Antonio and M. Freindorf, *Chem. Commun.*, 2023, **59**, 7151–7290.

114 E. Kraka, W. Zou, Y. Tao and M. Freindorf, *Catalysts*, 2020, **10**, 691.

## Data availability

The data supporting this article have been included as part of the Supplementary Information.